Laboratory studies into the effect of regolith on planetary X-ray fluorescence spectroscopy

Jyri Näränen, Hannu Parviainen, Karri Muinonen, James Carpenter, Kim Nygå Rd, Marko Peura

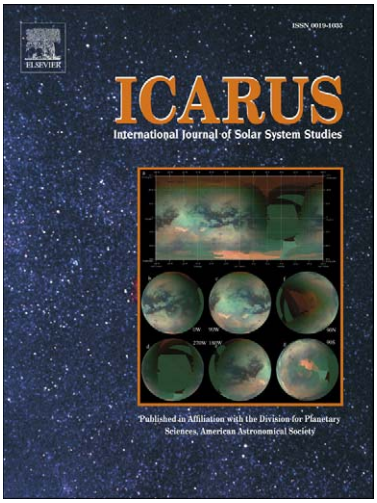

Laboratory studies into the effect of regolith on planetary X-ray fluorescence spectroscopy

Jyri Näränen, Hannu Parviainen, Karri Muinonen, James Carpenter, Kim Nygå rd, Marko Peura

PII: S0019-1035(08)00291-1
DOI: 10.1016/j.icarus.2008.08.004
Reference: YICAR 8742

To appear in: *Icarus*

Received date: 23 November 2007
Revised date: 31 July 2008
Accepted date: 5 August 2008

Please cite this article as: J. Näränen, H. Parviainen, K. Muinonen, J. Carpenter, K.N. rd, M. Peura, Laboratory studies into the effect of regolith on planetary X-ray fluorescence spectroscopy, *Icarus* (2008), doi: 10.1016/j.icarus.2008.08.004

Laboratory studies into the effect of regolith on planetary X-ray fluorescence spectroscopy

[1]Jyri Näränen, [1]Hannu Parviainen, [1]Karri Muinonen, [2]James Carpenter, [3]Kim Nygård, and [3]Marko Peura

E-mail: jyri.naranen@helsinki.fi

[1] Observatory, P.O. Box 14, FI-00014 University of Helsinki, Finland
[2] Space Research Centre, Department of Physics and Astronomy, University of Leicester, University Road, Leicester LE1 7RH, United Kingdom
[3] Department of Physical Sciences, P.O. Box 64, FI-00014 University of Helsinki, Finland

Submitted to *Icarus*
Submitted 23 November 2007
Revised 31 July 2008

Manuscript pages: 39
Tables: 3
Figures: 13

Proposed Running Head: Regolith effects on X-ray fluorescence spectroscopy

Editorial correspondence to:
Jyri Näränen
Observatory
P.O. Box 14
FI-00014 University of Helsinki
Finland
Phone: +358 9 191 21 773
Fax: +358 9 191 22 952
E-mail: jyri.naranen@helsinki.fi

Abstract

In the analysis of X-ray fluorescence spectra from planetary surfaces, it is traditionally assumed that the observed surface is a plane-parallel, smooth, and homogeneous medium. The spectral and spatial resolutions of the instruments that have been used to measure X-ray emission from planetary surfaces to date have been such that this has been a reasonable assumption, but a new generation of X-ray spectrometers will provide enhanced spectral and spatial resolutions when compared with previous instrumentation. In light of these improvements in performance, it is important to assess how the requirements on the methodology of analysis of spectra may change when the surface is considered as a regolith. At other wavelengths, varying physical properties of planetary regoliths, such as the packing density, are known to have an effect on the observed signal as a function of viewing geometry. In this paper, the results from laboratory X-ray fluorescence measurements of regolith analogue materials at different viewing geometries are presented. Characteristic properties of the regolith such as particle sizes and packing density are found to affect the measured elemental line ratios. A semiempirical function is introduced as a tool for fitting fluorescent line intensity dependences as a function of viewing geometry. The importance of the results is discussed and recommendations are made for the future analysis of planetary X-ray fluorescence data.

Key Words: ASTEROIDS, SURFACES; EXPERIMENTAL TECHNIQUES; MINERALOGY; MERCURY, SURFACE; REGOLITHS

1 Introduction

X-ray fluorescence spectrometers (XRFSs) are standard instruments in the typical suite used to study airless planetary bodies in the inner solar system from orbiting platforms. Since the days of the Apollo 15 and 16 missions, where the first XRFS data from another planetary body were obtained (Adler et al. 1972), the spatial and spectral resolution, and the overall sensitivity available for remote-sensing X-ray instruments, have improved substantially. After the Apollo era, XRFSs have been included in several orbiting planetary spacecraft payloads, including NEAR Shoemaker (Goldsten et al. 1997), SMART-1 (Grande et al. 2003), Hayabusa (Okada et al. 2006), and Kaguya (formerly Selene) (Okada et al. 2002). XRFSs will be included in the payloads of future missions such as Chandrayaan-1 (Joy et al. 2008), MESSENGER (Schlemm et al. 2007), and BepiColombo (Schulz and Benkhoff 2006).

The soft X-ray energy region may be considered to lie between approximately 0.5 and 10 keV. For planetary surfaces, fluorescent X-ray emission in this energy band occurs following the ionization of surface elements. For most planetary surfaces in the inner solar system, solar coronal X-rays are the primary cause for ionization. Additional ionization is due to impacting ions and electrons.

Planetary X-ray fluorescence spectroscopy provides elemental abundance maps of major rock-forming elements in the topmost layer ($\sim$10-100 μm) of regoliths on surfaces of planets and small bodies in the inner solar system (Adler and Trombka 1970). Elemental maps are invaluable for the geochemical study of the surface. Abundance maps provide information about a planet's surface geology and this in turn can be used to infer the planet's crustal evolution. This can also have implications for investigations into the bulk composition of a planet, therefor placing important constraints on its origin and evolution. The planet-meteorite connection can also be studied through X-ray fluorescence spectroscopy (Nittler et al. 2004).

Conversion from elemental abundances to rock types has thus far been carried out by comparing the data obtained by orbiting instruments with either results from laboratory spectroscopy or from numerically modeled spectra. Laboratory samples are normally slabs of rock samples with smooth surfaces and numerical simulations consider the surface to be a smooth, homogeneous, and plane-parallel medium.

The interactions of photons with the regolith, as opposed to an ideal surface, are known to result in large effects in visible-wavelength spectroscopy and photometry (e.g., Hapke 1965, Lumme and Bowell 1981). A recent review of the subject can also be found in Muinonen et al. (2002). These effects are related to characteristic parameters such as particle-size distribu-

tion, packing density (the integrated particle volume vs. the bulk volume of the sample), and surface roughness. Investigations by previous authors (description in more detail follows) into the effects on X-ray emission of particle size and surface roughness reveal analogous effects for fluorescent X-ray emission. Thus the analysis of X-ray fluorescence data from planetary missions requires that the approximation of the plane-parallel medium be developed further, to consider the surface as a regolith with varying physical properties.

In this paper, the effects due to regolith surface roughness and porosity as well as particle-size distribution on X-ray fluorescence emission are investigated experimentally. The term "regolith effects" is coined to envelop the effects produced by these physical parameters of the regolith. Some previous authors have defined their "surface-roughness effects" as being the same as the "regolith effects". In this paper the surface roughness, that plays probably the most prominent role in the regolith effects, is defined as being the undulating boundary between free space and the particulate medium in similar fashion as in Parviainen and Muinonen (2007). The present investigation shows that the measured intensity of a fluorescent X-ray line depend on both the measurement geometry and the physical properties of the regolith. Furthermore, it is shown that this effect is energy-dependent and cannot therefore be simply removed by taking the ratios of different elemental fluorescent lines, with different energies. It is the values of these elemental line ratios that have been mostly interpreted by previous authors when analyzing data from orbiting XRFSs.

In what follows, a review of previous investigations into regolith effects is given. In materials science, the effects of particle size on X-ray fluorescence have been studied both numerically and experimentally in an early article by Claisse and Samson (1962). They found that the increase of particle sizes in a medium decreases the measured fluorescent emission. This phenomenon was named the grain-size effect, a term that is widely used in geology and materials science. However, for this paper, the use of the term particle instead of grain is adopted, as the term particle describes better the semi-abstract nature of the particulate medium assumed in this study.

Later, Berry et al. (1969) reviewed Claisse and Samson's work as well as that of several others and introduced a treatment of packing density and the variation in the intensity of the elastically backscattered X-rays as a function of particle size. Hunter and Rhodes (1972) were among the first to introduce a continuous size distribution in their analytical formulation of the particle-size effect. An interesting phenomenon present in most of the abovementioned studies is the presence of a transition zone in the particle-size effect, i.e., the effect is most prominent within a fixed particle-size range of $\sim 10-300$ μm and almost non-existent outside of that range (McKay et al. 1991). For

regolith-type materials, the typical mean free path of X-rays in the medium corresponds well to the particle-size range of the transition zone. Planetary-regolith particle sizes lie also usually well within the transition zone.

Hawthorne and Gardner (1978) introduced a numerical model to simulate fluorescence from a medium consisting of cubic particles. Their model, which relied on numerical Monte-Carlo simulations, included varying incidence and emergence angles and non-random packing effects. They also performed laboratory experiments at several incidence angles and particle sizes to provide empirical validation for their modeling. Trucano and Batterman (1970) performed laboratory studies on how the porosity of a medium consisting of $\sim$100 μm glass spheres affects the X-ray scattering background as a function of viewing geometry. They observed a nonlinear viewing-geometry-dependent decrease (maximum $\sim$35%) of scattering from the porous medium when compared with a solid one.

These abovementioned studies are, however, of limited use for planetary missions because they either do not include changing viewing geometries, are performed assuming fixed geometries, or are concentrated on a single emission line.

The effect of regolith properties on X-ray fluorescence spectroscopy from orbital platforms around atmosphereless planets were examined in an early article by Hubbard and Keith (1977), who discussed the effects of surface roughness and particle size on the fluorescent emission of Si, Mg, and Al in Apollo 15 and 16 XRFS data. They showed that the Apollo 16 Si Kα intensity data as a function of illumination angle with nadir-observing geometry could be better fitted with simple photometric functions than with a cosine curve which calibrates the variation in solar intensity across the sunlit hemisphere of the target. They also suggested the existence of an effect reminiscent of the opposition effect in the visible wavelengths (Sidky Mikhail 1968). The Si Kα line in the Apollo data shows a $\sim$10% nonlinear increase in fluorescent intensity compared to their photometric model at phase angles $\pm$15° (phase angle, α, is defined as the angle between the observer and the light source as seen from the target surface). However, strictly, the opposition effect is within $\sim$10° phase angle, so they also included the backscatter effect caused by rough surface in their somewhat relaxed treatment of the opposition effect.

Regolith effects have been studied both numerically and in the laboratory by Maruyama et al. (2008), Okada (2002), Okada et al. (1998), and Okada and Kuwada (1997) for the calibration of orbital X-ray spectrometer data. They report a hardening (i.e., an increase in the higher-energy radiation over the lower-energy radiation) of the fluorescent X-ray spectrum as a function of increasing phase angle. This is mainly attributed to regolith effects. The simulated sample in their numerical ray-tracing model is a two-dimensional

rectangular wave characterized by two parameters that represents the rough surface produced by the granular nature of the regolith.

The present paper gives a brief overview of the physics of X-ray fluorescence spectroscopy and introduces a novel semi-empirical model for modeling the measured elemental line intensities at different phase angles. This is followed by a description of the laboratory measurements and samples used in the study. The results and their interpretation and comparison to those of previous studies are then presented. The paper ends with a discussion and conclusions that can be drawn from the results.

2 Theory

Below 10 keV the dominant interaction between incident X-rays and matter is photoelectric absorption. The energy required for photoabsorption from a particular shell is unique for each element. The subsequent filling of a core hole may result in the emission of a fluorescent X-ray, whose energy is characteristic for the electron transition that has taken place and is specific to the emitting element. The emerging fluorescent X-ray has always a lower energy than the incident X-ray that excited the fluorescence. The process in which fluorescent radiation itself is absorbed and reemitted as fluorescent radiation is called secondary fluorescence. The so-called Kα and Kβ fluorescence emission is due to filling of a 1s hole. Fluorescence is isotropic, i.e., fluorescent radiation has an equal probability to be emitted in any direction. X-ray spectra also contain scattered and diffracted X-rays, originating at the source and scattered from the regolith.

Figure 1 defines the angles used throughout this study. The surface interface between the regolith and the space is defined by the function $z_s = z_s(x, y)$. The principal plane is a plane where $\Delta\phi = \phi - \phi_0 = 180°$, where ϕ_0 and ϕ are the azimuth angles of the incident and emergent radiation, ι and ϵ, respectively. All of the studies reported here were performed in the principal plane, i.e., no azimuth effects were studied. As a further simplification, all of the measurements were performed with either $\iota = 0°$ or $\epsilon = 0°$, i.e., the angle that was not fixed coincided with the phase angle.

In what follows, a description of a semiempirical model for the tentative interpretation of the laboratory measurements, presented later in this paper, is given. The semiempirical modeling relates to the angular dependence at a given energy. The mathematical fitting parameters vary as a function of energy and fluorescence peak ratios can be computed from the energy-specific models.

Let us concentrate on a single emission line of a certain element. Fur-

thermore, let us assume a monochromatic source of incident radiation above the absorption edge of the emission line. As described earlier, the attenuation of the incident radiation in the medium differs from that of the emitted radiation. In radiative transfer, this difference manifests itself in differing optical depths as per physical distance in the directions of incident and emergent radiation. Considering solely a single absorption and emission process within the medium, the differing attenuation coefficients introduce wavelength-dependent constants in an otherwise Lommel-Seeliger-like denominator (Fairbairn 2005).

The coefficient of emission R corresponding to the reflection coefficient in visible-light photometry is of the form

$$R(\iota,\epsilon,\phi) \;=\; \frac{\beta_1}{\beta_1\cos\epsilon+\beta_2\cos\iota}P(\iota,\epsilon,\phi) \;=\; \frac{1}{\cos\epsilon+\frac{\beta_2}{\beta_1}\cos\iota}P(\iota,\epsilon,\phi), \quad (1)$$

where $P = P(\iota,\epsilon,\phi)$ is the phase function describing regolith effects, and β_1 and β_2 are the linear attenuation coefficients for the energy of the incident radiation and the energy of the emission line.

If a linear phase-angle (α) dependence is assumed for P, the fluorescent emission R can be modeled as

$$R(\iota,\epsilon,\phi) = \frac{R_0}{\cos\epsilon+\eta\cos\iota}(1+k\alpha). \quad (2)$$

Here a constant scale factor R_0, the slope of the phase function k, and the ratio of the attenuation coefficients $\eta = \frac{\beta_2}{\beta_1}$ are introduced as free parameters to be fitted to the data.

The relation between the observed power from a sample integrated over the detector area and the incident unidirectional radiation is now

$$I(\iota,\epsilon,\phi) \sim \cos\epsilon R(\iota,\epsilon,\phi). \quad (3)$$

Thus, finally, the semiempirical model for the observed power, which can be linearly fitted to the intensities measured as shown in Sect. 4, should behave as

$$I(\iota,\epsilon,\phi) \sim \frac{R_0\cos\epsilon}{\cos\epsilon+\eta\cos\iota}(1+k\alpha). \quad (4)$$

The results from these models semiempirical in the angles have been verified against two different numerical codes. First, a straightforward numerical integration of the radiative-transfer equation was implemented. Next, a more involved Monte-Carlo ray-tracing simulation was implemented and tested against the semiempirical and numerical models. The results given by the numerical models agree accurately with the semiempirical model.

3 Laboratory measurements

Planetary regoliths can be approximated in the laboratory by analogue materials from terrestrial sources. For most terrestrial planets, the study of analogues provides the only means of supporting remote sensing with laboratory measurements. Lunar regolith samples obtained by the Apollo and Luna programmes and the few meteorites, whose parent bodies have been identified, are the only exceptions.

In the present study, a lunar mare regolith analogue was chosen for analysis. The measurement geometries reproduce some of the most relevant geometries encountered in orbiting spacecraft observations, i.e., nadir pointing and zenith illumination at off-nadir observing conditions.

3.1 Soft X-ray spectrogoniometer

The experimental setup used in the present study was originally designed for the ground calibration of the X-ray Solar Monitor (XSM) of the European Space Agency SMART-1 lunar mission (Huovelin et al. 2002). The goniometric, i.e., angle-measuring, setup was designed specifically for the study of the viewing-geometry-related effects caused by regolith properties presented in this paper. The spectrogoniometer consists of a cylindrical chamber which can be pumped into near-vacuum (4 mbar) to reduce the effects (absorption, scattering) of air on the measured signal, which make measurements at $\lesssim$ 5 keV difficult to perform at normal temperature and pressure (NTP) conditions (see Fig. 2 for illustration of the experiment). The detector used for the measurements was a laboratory replica of the abovementioned XSM instrument. The detectable energy range for the detector is 1-20 keV and spectral resolution $\sim$250 eV at 6 keV. The X-ray source used in the experiment is a sealed and air-cooled Ti-anode miniature X-ray tube (Oxford X-ray Technologies Inc. Model XTF-5011) with a 75 μm thick Be window. The window limits the usable soft X-ray output to above 1 keV. The voltage applied to the X-ray tube was 25 kV and the current was 0.5 mA. The exact shape of the incident X-ray source spectrum cannot be measured due to detector restrictions. However, a semi-empirical spectrum of the X-ray source was constructed in a similar fashion as in Ebel et al. (1989) for estimating the change in the measured relative elemental line ratios as a function of the viewing geometry for plane-parallel homogeneous medium, as discussed in Sect. 4.1. The semi-empirical spectrum is shown in Fig. 3.

The incident X-ray beam was collimated by two slits of changeable sizes. Different X-ray beam sizes were applied in search of an optimum signal-to-noise/beam size ratio. If the angular size of the X-ray beam as seen from the

sample surface is too large, it can average out some of the viewing-geometry effects. Also, if the X-ray beam footprint on the sample surface is too large it may grow larger than the sample as the angle of incidence increases making studies of absolute intensities impossible. The largest beam size used was 2 mm×8 mm (2 mm wide in the plane of the movement of the goniometer, i.e., the principal plane of the viewing geometry). This translates into a ∼0.2° angular diameter as seen from the sample surface and ∼0.4° beam footprint size on the sample as seen from the detector. However, smaller beam sizes were also applied in a search for optimal integration time. Integration times were 4-8 hours in each viewing geometry, depending on the incident X-ray beam size used.

The data acquisition and the movements of the goniometer were controlled by Spec software. The X-ray spectrum was read from the detector with a 2048 channel ISA-bus multi-channel analyzer (MCA) card.

The sample was either fixed normal to the direction of the light source or was rotated with the detector such that the sample-detector angle was fixed. The accessible phase-angle range was 7-51°, constrained by the geometry of the experimental setup.

The viewing geometries chosen to be measured were $\epsilon = 0°$ (i.e., the pointing direction of the detector was always towards the surface of the sample, thus simulating a nadir-pointing space instrument) and $\iota = 0°$ (i.e., the direction of incident X-rays was always towards the surface normal). Measurements were performed in angular increments of 2°.

3.2 Sample material

The lunar regolith analogue used in this study was an olivine-rich basalt, which was ground into a powder and then sieved to separate particles of different sizes. Powdered basalt with particle-size ranges of < 50 μm and $75 - 250$ μm, were used. A comparison of the analogue's composition and that of a lunar basalt is shown in Table 1. The particle-size distribution within these size ranges is unknown. The typical lunar regolith particle-size distribution has been measured to have a median at ∼70-100 μm with ∼10% of the material smaller than 10 μm, and near-surface packing density of ∼50% (McKay et al. 1991, Costes et al. 1970). The sample material with larger particle sizes fits well in the lunar particle-size region.

The particle-size range in the sample with finer particle sizes corresponds closely to the particle-size distribution in hermean regolith which have a median at ∼30 μm (Warell and Blewett 2004), even though the chemical composition of the hermean regolith is unlikely to be close to olivine basalt. The sample material with larger particle sizes has also been used in a study

of the opposition effect observed in the visible wavelengths (Näränen et al. 2004).

Because the samples need to be oriented vertically and measured in near-vacuum, all of the samples were pressed into a pellet format commonly used for X-ray analyses of rock samples. Compression of the samples resulted in an average sample density of 2.13 g/cm^3. Compared to the density of basalt, 2.9 g/cm^3, this results in packing density of $\sim$0.74. The packing density of the pellets is significantly larger than that expected for a plausible planetary-regolith analogue.

3.3 Data reduction and analysis

The data, as received from MCA, is calibrated for energy scale in IDL. In the calibration, the knowledge of the positions of the identified emission peaks in the data, known *a priori*, is used to perform a χ^2 linear fitting for transforming the channel numbers into the energy scale.

The data is then converted into the Flexible Image Transfer System (FITS) format for exporting it to XSPEC (Arnaud 1996). The redistribution matrix (RMF) and auxiliary response (ARF) files are also constructed to allow absolute calibration of the spectra. The input for these two files is provided by the flight calibration data for the XSM since the detector used in this study is a laboratory replica of that instrument (Lauri Alha, private communication, 2007).

The energy region to be processed was chosen to be 3.0-7.5 keV. The signal-to-noise ratio of the data was unacceptably low below 3 keV due to relatively low vacuum achievable with the vacuum chamber used in this study (causing scattering and absorption at small energies) as well as the low quantum efficiency and low resolution of the detector at small energies. Above 7.5 keV, there were no detectable fluorescent lines.

A total of nine emission lines were identified and modelled using a combination of nine one-dimensional Gaussian profiles (see Fig. 4). XSPEC provides an iterative fitting routine, in which the model parameters (in this case the line center and the energy contained within the line) are changed by small steps and the resultant model is then compared with the data. The comparison is done by the χ^2 method and the fitting is continued until the optimum χ^2 solution is found. Normally, the reduced χ^2 numbers were 1.4$\pm$0.5. For several spectra, the reduced χ^2 values of the fits were noticeably larger than the mean value for the fits and the fits were deteriorated by several noisy channels in the data, whose origin could not be deduced. These spectra were not included in the final analysis of the data.

When the optimal fit was found, the 1σ confidence levels for the derived

line intensities were calculated. Both the Poissonian statistics (shot noise) and the uncertainties in the fitting of the lines were taken into account in the calculation of the confidence levels.

It is worth noticing that fitting lines to the spectrum is quite sensitive to the other lines close by. For example, in the measured spectra, K Kα, and most importantly Ti Kα lines are close to and overlapping Ca Kα. For several very distinguishable angles that varied for different samples and viewing geometries, the Ti Kα line exhibited a strong increase in intensity when compared to intensities of other lines in the spectrum. There is some Ti in the sample material, but most of the measured Ti Kα is backscattered Ti-anode X-ray tube radition. However, because the X-ray incident beam was collimated to a narrow beam, X-ray diffraction is also expected to be seen at specific angles, especially at the Ti Kα energy (Dr Graeme Hansford, private communication 2008). The observed increase in Ti Kα was attributed to X-ray diffraction. For the angles where the diffraction took place, the measured Ca Kα intensities were slightly smaller due to errors in the way the fitting routine accommodated the enhancement of Ti Kα. Ca Kα line intensities of these angles were chosen not to be included in the present study.

The spectra are individually processed in XSPEC to obtain deconvolved fluorescent emission lines for the different elements. Figure 4 illustrates the spectrum as seen by the detector. Figure 5 contains the emission lines corrected for the detector characteristics (such as the effective area at different energies etc.).

4 Results

The measured elemental line intensities for which the best signal-to-noise ratios were obtained were Ca Kα, Fe Kα, and Fe Kβ, and these lines are used for the following analyses. Iron and calcium are two of the most important rock-forming elements observable by planetary XRFSs. The 1σ confidence ranges for the measurements are represented as error bars in the figures depicting the results.

4.1 Relative elemental line ratios

Historically, most of the measurements of X-ray emission lines by XRFSs on planetary missions are expressed as the relative abundancy ratios of two elements, obtained by ratioing the measured fluorescent line intensities of the elements. The calibration process needed to obtain relative elemental ratios is simpler than for obtaining absolute elemental abundances since by ratioing

one can remove energy-independent effects caused by gross compositional and physical variations in the regolith.

The results of these experiments seem to exhibit nonlinear behaviour at the smallest angles (for both incidence and emergence angles) and this may be due to the existence of an opposition effect, as suggested by Hubbard and Keith (1977). Therefore, the relative line intensities presented here were chosen to start at 9° and not at 7° which was the smallest angle of the measurements.

In Figs. 6 and 7, the relative intensities of Ca Kα, Fe Kα, and Fe Kβ measured with $\epsilon = 0°$ of both samples are presented. The data have been fitted with a linear function of the form $y = A + Bx$ to provide a qualitative tool for comparing the results. As the angle of incidence increases, the relative strength of the Fe Kα emission line also increases relative to that from Ca Kα. However, when comparing Fe Kβ and Ca Kα the effect is reduced and, when comparing Fe Kβ and Fe Kα, the trend for hardening of the elemental ratios is reversed.

The observed reverse of the effect for Fe Kβ/Kα is attributed to fluorescence being a two-fold phenomenon. The incident radiation that excites the fluorescence from the K-shell, is the same for both of the emission lines since the photoabsorption takes place in the same shell (in this instance Fe 1s). However, the emergent Kβ and Kα fluorescent radiation have different penetration depths in the medium, allowing more Kβ radiation to emerge from the medium. This also results in a difference in Fe Kα and Kβ line ratios to Ca Kα. The measured relative elemental line ratios contain some scatter which may be attributed primarily to Ti diffraction and errors in deriving the elemental line intensities from the spectra as discussed in the previous section. Fe Kβ data is presented here as a control measurement for the analysis for that scatter. If the scatter was caused by, e.g., contamination of external Fe K-line emission or some other systematic source for error, both Fe Kα and Kβ lines would be affected in a similar fashion. However in Figs. 6-9 it can be observed that the Fe Kα and Kβ relative line ratios to Ca Kα do not experience similar kind of scatter although, for some angles, the trend in the scatter is similar and is most probably related to errors in fitting Ca Kα. There are, however, many angles were the behaviour of the relative line ratios are different. This is due to errors in fitting of Fe Kα and Kβ lines.

XRFS observations in planetary missions are typically performed with a nadir pointing aperture ($\epsilon = 0°$). However, off-nadir observation geometries with $\epsilon \neq 0°$ may also occur and it is therefore useful to study this geometry as well. The elemental line ratios as functions of the emergence angle are shown in Figs. 8 and 9.

The viewing-geometry-related effect is different in this measurement ge-

ometry. Now, as the angle of emergence increases, the relative strength of Fe Kα emission decreases when compared to Ca Kα emission, i.e., the spectrum softens. When comparing Fe Kβ and Ca Kα the effect is smaller and when comparing Fe Kβ and Fe Kα it is actually reversed.

For quantitative analysis of the line-intensity-ratio changes, only the Fe Kα/Ca Kα line ratio was chosen to be presented. The effects are basically the same for Fe Kα/Ca Kβ, only somewhat smaller because of the change in the line ratio of Fe Kβ/Fe Kα explained above. Also the signal-to-noise was a lot poorer for Fe Kβ than for Fe Kα and Ca Kα. Results of the linear fitting of Fe Kα/Ca Kα line ratios for all the samples in both viewing geometries is given in Table 2 and a more thorough discussion on the relative change of this line ratio is given below.

X-ray fluorescence from a homogeneous plane-parallel surface can be predicted from fundamental physical parameters, as discussed in, e.g., Criss and Birks (1968). This approach has been dubbed as "the fundamental-parameters method" or "the fundamental-parameters equation" of energy-dispersive X-ray spectroscopy, which is somewhat misleading since it does not take into account, e.g., the fundamental physical parameters describing the medium. However, since the terminology is well established in X-ray research, in this paper it is used as well. Such a theoretical treatment of fluorescence predicts a change in the observed relative elemental line ratios, as a function of off-axis angle, even without the inclusion of regolith effects. This can be qualitatively described as follows: the photoabsorption and subsequent fluorescent emission of higher-Z elements statistically takes place deeper in the material than for lower-Z elements. Fluorescent radiation has smaller penetration depths in the material than the incident radiation that excited it. For monochromatic exciting radiation, this causes hardening, i.e., enhancement of the higher-energy lines of the fluorescent spectrum as a function of growing emergence angle ($\iota = 0°$) and softening as a function of growing incidence angle ($\epsilon = 0°$). For non-monochromatic X-ray sources, as is the case in the present study which utilizes a Ti-anode X-ray tube (see Fig. 3), the situation becomes more complicated and is not easily explained qualitatively. Either softening or hardening of the spectrum can occur for all measurement geometries, depending on the elemental composition of the sample and the spectral shape of the exciting radiation. In X-ray analysis the effect expected for plane-parallel homogeneous medium can be taken into account by either using a smooth, solid, sample as the calibration standard or by numerical simulation. The latter approach was attempted in this paper as no smooth enough solid samples of the olivine-basaltic composition were available.

In the present study, it is observed that samples with different particle

size ranges display different amounts of relative elemental line ratio change. This is due to effects caused by the physical properties of the regolith that are superposed to the relative elemental line ratio change predicted by the fundamental-parameters approach, which should be the same for both samples.

Several physical parameters of the regolith, such as packing density and particle-size distribution, produce together surface roughness in the topmost layer of the regolith. Since the fluorescent emission is produced in the first tens of micrometers of a medium, it is safe to assume that the most dominant physical parameter of the regolith (apart from its chemical composition) affecting the observed X-ray spectrum is this surface roughness. In the angular region where the opposition effect takes place, i.e. $\alpha < 10°$, also the surface porosity may have an effect.

Surface roughness in a regolith can either shadow the incident radiation (for $\epsilon = 0°$) or it can shield the emergent radiation (for $\iota = 0°$). In both cases, the effect has a higher probability at lower energies and is more pronounced at large angles. In shadowing, the higher-energy fluorescent emission (with longer penetration depths) has a higher probability of emerging towards the detector from areas shadowed by the roughness of the surface than the lower-energy emission. In shielding, the direction of the radiation is reversed, but the effect is essentially the same. Both of these effects depend on the shape of the incident radiation spectrum and should thus be addressed individually in the modelling of the regolith effects instead of treating the effects solely as a function of the phase angle.

In Fig. 10, the changes in the relative line ratios of Fe Kα/Ca Kα for both samples are compared as a function of illumination angle ($\epsilon = 0°$) and, in Fig. 11, as a function of emergence angle ($\iota = 0°$). Results obtained by fitting a linear function of the form $y = A + Bx$ to the data alongside the fitting parameter values and their error estimates and reduced χ^2 values of the fits are presented in Table 2. In Fig. 10, the sample with larger particle sizes exhibits a larger relative change. The linear fit indicates an increase of 8.5% in the line ratio of Fe Kα and Ca Kα over the incidence-angle range of 0-50° for the sample with larger particle sizes and 4.2% for the smaller-particle sample. The values of the slope parameter B for the two fits do not overlap within their 1σ confidence ranges and if the data of one sample is fitted with the slope value of the other the χ^2 value of the fit is more than twice that of the optimal solution thus providing confidence that the measured relative line ratio changes are actually different for the different samples.

If it is assumed that a smaller-particle sample pellet has a smoother surface than the larger-particle sample pellet, then the difference is explained by the shadowing induced hardening of the spectrum caused by the larger

amount of surface roughness in the sample with coarser particle sizes. As explained in Sect. 3.1., the exact shape of the X-ray source spectrum could not be measured directly and was estimated using a semi-empirical model. This model was used as the input spectrum in a numerical simulation performed using a fluorescence code at the University of Leicester Space Research Centre. The code utilized the fundamental parameters equation (Clark and Trombka 1997) to estimate the elemental line intensities emerging from a plane-parallel homogeneous medium of olivine-basaltic composition. For $\epsilon = 0^\circ$ measurement geometry, the relative line intensity ratio of Fe Kα/Ca Kα increased by 3% over the incidence-angle range 0-50°. This is quite close to the change measured of the sample with smoother surface, and would leave $\sim 5\%$ as the contribution of the regolith effects for the sample with rougher surface. However, one should exercise caution when doing this comparison quantitatively as the exact shape of the X-ray source is not known.

The roughness and porosity in pellet-type sample surfaces has been studied using SEM imaging (Näränen et al., paper under preparation) and it has been found that pellets with smaller particles have much smoother surfaces, i.e., are closer to being a homogeneous plane-parallel medium, than pellets with larger particles. Due to sample preparation by compressing the pellets in a press, the particles in both pellets are preferentially horizontally oriented. However, the samples with larger particle sizes are packed less efficiently leaving the surface more porous and ragged in appearance.

This also agrees with the comparison shown in Fig. 11 where the relative change is actually smaller for the sample with larger particles (rougher surface). The change is -2.0% for the rougher sample over the emergence-angle range of 0-50° and -7.7% for the smoother sample. The relative change in line ratios obtained from the numerical simulation of the fundamental parameters equation is -6%, again quite close to the value obtained with the smoother sample and leaving $+4\%$ as the contribution of the regolith effect for relative line ratio change measured with the rougher sample. This 4% is explained by the shielding of the fluorescent radiation from the detector field of view by the surface roughness. Shielding enhances the higher-energy end of the spectrum in a fashion similar to shadowing. Similar to the case of $\epsilon = 0^\circ$, the slope values do not overlap within their 1σ confidence ranges and interchanging the slope values produces considerably poorer fits.

The samples studied in this paper are compressed to pellets, and are thus inherently closer to being plane-parallel than uncompressed materials. It may be suggested that the regolith effects are larger for uncompressed samples, such as planetary regoliths.

4.2 Absolute line intensities

To understand the physical phenomena responsible for the relative line-intensity-ratio change, the intensities of the separate elemental lines need to be studied as a function of the viewing geometry.

In Figs. 12 and 13, the absolute line intensities of Fe Kα and Ca Kα are presented, with the best fit achieved with the semiempirical function of Eq. 4. The fitting parameters are enumerated in Table 3 with their 1σ errors. A reduced χ^2 value is also given for the fits.

The results presented here are obtained in a measurement geometry for a sample with a planar geometry. The incident beam size was fixed during the measurement and the detector field of view was always larger than the illuminated surface of the sample. For planetary X-ray fluorescence spectroscopy, the instrument field can encompass an extended area from a spherical body, and the observed intensity is integrated over many values of ι and ϵ.

While a considerable simplification of the true complex processes occurring in the fluorescent medium, a Lommel-Seeliger-type model based on radiative transfer (Eq. 1) is observed to fit the trend in the observed absolute line intensities well. For some measurements, the semiempirical function does not fit the angles below 10° well. This may be due to the presence of a shadow-hiding opposition effect caused by the surface roughness, similar to that observed at visible wavelengths.

The ι dependence arises from the inverse relation between the mean free path of a photon and the attenuation coefficient β. The greater the incident angle, the smaller the depth in the medium, normal to the surface, in which a photon is likely to be absorbed. For an increasing angle of incidence, the fluorescence will take place closer to the surface of the medium, and the number of photons emitted from the medium is increased. The ϵ dependence results from the change in the projected optical depth. As ϵ increases, the projected optical depth from a layer of given thickness increases. Since the fluorescent radiance from the layer decreases with the increasing thickness of the layer, the emergent radiance increases as a function of increasing ϵ. Finally, since the area of the sample projected to the imaging plane of the detector decreases as a function of ϵ as $\cos\epsilon$, the observed power integrated over the imaging plane follows the Lommel-Seeliger-type model multiplied by $\cos\epsilon$.

The results from fitting the semiempirical function (Eq. 4) to the absolute line intensities was also used to fit the relative elemental line ratios measured as a function of the viewing geometry, as discussed in the previous section. The resultant fits, although somewhat nonlinear, produced χ^2 values that are comparable to those of the linear fits used in the study of the regolith effects

in the previous section. A more thorough study on the propagation of the confidence ranges of the parameters of the semiempirical function into the study of the line intensity ratio changes is needed before the semiempirical function can be utilized in studying, and ultimately, in predicting change in elemental line ratios as a function of the viewing geometry. This remains as a topic for future studies.

4.3 Comparison with previous studies

Näränen et al. (2007) introduced new Monte-Carlo ray-tracing simulations of the effect of regolith properties on fluorescent X-ray emission. All of the simulations reported there were performed with an illumination source fixed in a direction normal to the surface (i.e., $\iota = 0°$). A strong correlation between the intensity of fluorescent X-rays and particle size was observed in the simulations, with the smallest particles producing the greatest fluorescent intensity. An opposition effect, i.e., a nonlinear brightening, was also observed to arise at small phase angles ($< 10^{\circ}$). This was attributed to a shadow-hiding mechanism that also partly causes the opposition effect at visible wavelengths. The results are in qualitative agreement with the results of the present study.

Okada (2002) measured relative line ratios of Ca, Fe, and Ti of loose-powdered basalt samples of four different particle sizes over phase-angle range of 21-76° ($\iota = 45°$) to study the effect of particle sizes. In his study he utilized an experimental setup consisting of a helium chamber, a Cr-anode X-ray source, and a semiconductor X-ray detector. It is not clear how he separated the change of relative elemental line ratios expected for the plane-parallel homogeneous medium and the effect caused by the different particle size ranges in the samples. However, in a later paper by the same research group (Maruyama et al. 2008), the use of a smooth, solid, calibration sample of the same elemental composition as the powder samples is indicated. It is thus assumed that the two effects are separated in the results by Okada and only the latter is reported. He reports a decrease of Ca/Fe relative line ratio (i.e., hardening of the spectrum) as a function of increasing phase angle for all the samples, with larger decrease for samples with larger particles and almost zero for the smallest particles (smoothest surface). The decrease was 12 and 6 % for samples with particle-size ranges of 106μm-180μm and >180μm, respectively, over the phase-angle range of 21-50%. These particle-size ranges are in the same general range as in the rougher sample used in the present study. The effect was smaller for Ca/Ti as is expected if the regolith effects are more effective for higher energies.

For the measurements reported in the present paper, if the change ex-

pected from the fundamental parameters equation is assumed to be reliably calculated using the semi-empirical model for the X-ray tube spectrum (see discussion in Sect 4.1.) the remaining contribution of the regolith effects as a function of the phase angle would be ∼0% for the smoother sample (similar to the result presented by Okada) and ∼4% (hardening) for the rougher sample over the phase angle range of $0 - 50°$, regardless of the measurement geometry. The discrepancy in the amounts of hardening reported here and those of Okada for the samples with larger particles is most likely due to the samples used in the present study being compacted pellets where less surface roughness and hence less regolith effects are to be expected.

Maruyama et al. (2008) reported results of a numerical simulation on the regolith effects or particle-size effect as they call it. They assumed an average particle size of 75 μm and typical soil composition at Apollo 12 site. They estimated a decrease of a few percent in Mg/Si and Al/Si over the incidence-angle range of 35-75°; the decrease was slightly larger for Mg/Si. This is in qualitative agreement with the results of the present study and also with the results by Okada (2002).

Although the studies by Okada and Maruyama et al. utilized loose powder samples for which the regolith effects would be expected to be larger, the results of the present study and the abovementioned authors' agree qualitatively very well. Larger particles in the sample, i.e., rougher surface is seen to increase the hardening of the spectra as a function of growing phase angle.

In their analysis of the X-ray spectra from the NEAR Shoemaker X-ray spectrometer (XRS), Nittler et al. (2001) identified H or R chondrites as the most likely meteoritic analogue for asteroid 433 Eros, although lower-iron L or LL ordinary chondrite subclasses were also deemed possible. L or LL chondritic composition was independently suggested by the NEAR gamma-ray spectrometer (GRS) experiment (Evans et al. 2001). The main mismatch between the results with the XRS and the GRS was that the GRS measured a significantly lower Fe/Si intensity ratio than the XRS. The difference in the elemental ratios measured by the XRS and the GRS experiments is ∼50% and the uncertainties in the data presented for both channels do not overlap. GRS sampled the target composition tens of cm below the surface whereas the XRS sampled the topmost $\sim 100\mu$m of the surface. Thus, it is possible that the mismatch is related to the different sampling depths and is caused by, e.g., geomechanical factors affecting the regolith on 433 Eros such as the "Brazil-nut effect" (Rosato et al. 1987) or the "reverse Brazil-nut effect" (Hong et al. 2001). These effects could potentially alter the surface composition as a function of depth.

Okada (2002) re-examined the results from the XRS in the light of possible viewing-geometry-dependent regolith effects (NEAR obtained most of its

data at large phase angles). Okada arrived at the conclusion that when the regolith effects are accounted for in XRS analysis, the L or even LL chondritic composition becomes the most likely meteoritic analogue for 433 Eros. The studies reported in this paper qualitatively support his conclusion. Regolith surface roughness tends to harden the spectrum as a function of increasing phase angle. Thus an elevated Fe/Si intensity ratio would be expected. Also the regolith effects would be most notable with the Fe/Si intensity ratio since the regolith effects are expected to become larger for higher energetic fluorescent lines. Most likely the regolith effects are not the only mechanism resulting in increased measured iron content, but it could explain it at least partly. It is worth noting that the gamma ray measurements are not affected by the same small-scale surface roughness effects as the X-ray measurements. Gamma rays are produced by interaction of the cosmic background radiation with the regolith and the cross section of absorption of gamma rays in the regolith is small. Also, several possible explanations were given for the low iron content measured with the GRS (Evans et al. 2001) thus bringing the results from the GRS measurements closer to those obtained by the XRS.

5 Discussion

The measurements presented here show effects of illumination and observation geometries and surface roughness on the intensity of fluorescent X-rays emerging from the planetary regolith at different energies. The measurements, performed using lunar regolith analogues, cannot currently be used for the validation of conclusions drawn from numerical modelling. Analogue materials are heterogeneous in composition and are not easily simulated. A future goal should therefore be to characterize analogue samples sufficiently that their properties and inhomogeneities can be properly accounted for in the numerical simulations. A possible future sample for analysis might be a well-defined mixture of two or three different kinds of spherical particles of single elements which can be more easily modelled. Also, the X-ray source spectrum should be better characterized. A more detailed quantitative analysis of the structure of the samples would be beneficial for modelling. For example, X-ray tomographic images of the sample would provide insight into the packing density and roughness of the pellet surface. Two-dimensional mapping by energy-dispersive X-ray spectroscopy (EDX) in a scanning electron microscope would provide information on the extent of elemental inhomogeneity of the samples. The semiempirical function presented in this paper may be utilized to study the change in the relative line intensities. A linear function was found to be a satisfactory initial approach in studying the

elemental line ratio changes as a function of the phase angle and especially in demonstrating the existence of the regolith effects. The utilization of a semiempirical function, such as Eq. 4, in the study and prediction of regolith effects for elemental line ratios remains as a future goal, as discussed in Sect. 4.2. It is predicted that with a better understanding of the propagation of the parameter errors of the semiempirical function into elemental line ratios, the semiempirical function will prove to be a better tool for the study and prediction of the regolith effects on relative line intensity ratio changes than the linear function.

Several strategies can already be envisaged for planetary X-ray fluorescence spectroscopy to help account for the effects measured here in the laboratory. Firstly, if measurements are obtained at small phase angles then the regolith effects studied in the present paper will be small. However, at small phase angles the opposition effect can affect the measured spectra. The extent of the opposition effect in soft X-ray energy region remains as a topic for future studies. Secondly, the effects can be accounted for by introducing correcting functions of the regolith effects in the analysis of spectra. Measurements that are not calibrated for the regolith effects can be synthesized into a line intensity-phase-angle curve that can fitted with a function similar to Eq. 4 presented in this paper. If the relation between the parameters of the fit and the regolith characteristics are understood, information on some of the physical parameters of the surface, such as porosity, packing density, and particle-size distribution, can be obtained. This information, although necessarily restricted in the spatial resolution due to the scanning nature of planetary X-ray data acquisition, may help to select the most likely parameters for physical properties of the regolith obtained through other investigations.

6 Conclusion

The intensities of the fluorescent elemental X-ray lines observed from a regolith vary as a function of viewing geometry and physical parameters of the regolith in a way that cannot be explained by models of homogeneous plane-parallel medium. This must be taken into account when calibrating data that has a spatial resolution sufficient to allow well-defined viewing geometries. With a robust model of the regolith effects, it may also be possible to use multiangular X-ray fluorescence spectroscopy as an independent tool for determining some of the physical parameters of the regolith.

Acknowledgements

The research has been supported by the Academy of Finland. JN is grateful to the University of Helsinki Chancellor for travel grant. Dr Derek Pullan, Space Research Centre, University of Leicester and the Planetary Analogue Field Studies Network is recognized for providing the sample material with smaller particles. Dr Graeme Hansford, Space Research Centre, University of Leicester is acknowledged for help in understanding X-ray diffraction in olivine. JN would like to thank Lauri Alha for providing insight into the X-ray detector physics and also for help in the data analysis. Dr Juhani Huovelin is acknowledged for providing the flight spare of XSM for use in this study. This paper was improved significantly by the helpful comments from the reviewers Dr Tatsuaki Okada and Dr Lucy Lim.

References

Adler, I. and Trombka, I. J. (1970), *Geochemical exploration of the moon and planets*, Berlin: J. Springer, 1970.

Adler, I., Trombka, J., Gerard, J., Lowman, P., Schmadebeck, R., Blodget, H., Eller, E., Yin, L., Lamothe, R., Gorenstein, P. and Bjorkholm, P. (1972), 'Apollo 15 geochemical x-ray fluorescence experiment: Preliminary report', *Science* **175**, 436–440.

Arnaud, K. A. (1996), Xspec: The first ten years, *in* G. Jacoby and J. Barnes, eds, 'Astronomical Data Analysis Software and Systems V', Vol. 101, Astronomical Society of the Pacific, p. 17.

Berry, P. F., Furuta, T. and Rhodes, J. R. (1969), 'Particle Size Effects in Radioisotope X-ray Spectrometry', *Advances in X-ray Analysis* **12**, 612–632.

Claisse, F. and Samson, C. (1962), 'Heterogeneity effects in X-ray Analysis', *Advances in X-ray Analysis* **5**, 335–354.

Clark, P. E. and Trombka, J. I. (1997), 'Remote X-ray spectrometry for NEAR and future missions: Modeling and analyzing X-ray production from source to surface', *Journal of Geophysical Research* **102**, 16361–16384.

Costes, N. C., Carrier, W. D., Mitchell, J. K. and Scott, R. F. (1970), 'Apollo 11 soil mechanics investigation', *Science* **167**, 741.

Criss, J. W. and Birks, L. S. (1968), 'Calculation methods for fluorescent x-ray spectrometry. empirical coefficients versus fundamental parameters', *Analytical Chemistry* **40**, 1080–1086.

Ebel, H., Ebel, M. F., Wernisch, J., Poehn, C. and Wiederschwinger, H. (1989), 'Quantification of continuous and characteristic tube spectra for fundamental parameter analysis', *X-ray Spectrometry* **18**, 89–100.

Evans, L. G., Starr, R. D., Brückner, J., Reedy, R. C., Boynton, W. V., Trombka, J. I., Goldstein, J. O., Masarik, J., Nittler, L. R. and McCoy, T. J. (2001), 'Elemental composition from gamma-ray spectroscopy of the NEAR-Shoemaker landing site on 433 Eros', *Meteoritics and Planetary Science* **36**, 1639–1660.

Fairbairn, M. B. (2005), 'Planetary Photometry: The Lommel-Seeliger Law', *Journal of the Royal Astronomical Society of Canada* **99**, 92–93.

Goldsten, J. O., McNutt, Jr., R. L., Gold, R. E., Gary, S. A., Fiore, E., Schneider, S. E., Hayes, J. R., Trombka, J. I., Floyd, S. R., Boynton, W. V., Bailey, S., Brueckner, J., Squyres, S. W., Evans, L. G., Clark, P. E. and Starr, R. (1997), 'The X-ray/Gamma-ray Spectrometer on the Near Earth Asteroid Rendezvous Mission', *Space Science Reviews* **82**, 169–216.

Grande, M., Browning, R., Waltham, N., Parker, D., Dunkin, S. K., Kent, B., Kellett, B., Perry, C. H., Swinyard, B., Perry, A., Feraday, J., Howe, C., McBride, G., Phillips, K., Huovelin, J., Muhli, P., Hakala, P. J., Vilhu, O., Laukkanen, J., Thomas, N., Hughes, D., Alleyne, H., Grady, M., Lundin, R., Barabash, S., Baker, D., Clark, P. E., Murray, C. D., Guest, J., Casanova, I., D'Uston, L. C., Maurice, S., Foing, B., Heather, D. J., Fernandes, V., Muinonen, K., Russell, S. S., Christou, A., Owen, C., Charles, P., Koskinen, H., Kato, M., Sipila, K., Nenonen, S., Holmstrom, M., Bhandari, N., Elphic, R. and Lawrence, D. (2003), 'The D-CIXS X-ray mapping spectrometer on SMART-1', *Planetary and Space Science* **51**, 427–433.

Hapke, B. W. (1965), 'Laboratory Photometric Studies Relevent to the Lunar Surface.', *Astronomical Journal* **70**, 322.

Hawthorne, A. R. and Gardner, R. P. (1978), 'A Proposed Model for Particle-size Effects in the X-ray Fluorescence Analysis of Heterogenous Powders that Includes Incidence Angle and Non-random Packing Effects', *X-ray Spectrometry* **7**(4), 198–204.

Hong, D. C., Quinn, P. V. and Luding, S. (2001), 'Reverse Brazil Nut Problem: Competition between Percolation and Condensation', *Physical Review Letters* **86**, 3423–3426.

Hubbard, N. J. and Keith, J. E. (1977), Reevaluation of the Apollo orbital X-ray fluorescence data, *in* R. B. Merril, ed., 'Lunar and Planetary Science Conference', Vol. 8 of *Lunar and Planetary Science Conference*, pp. 909–923.

Hunter, C. B. and Rhodes, J. R. (1972), 'Particle Size Effects in X-ray Emission Analysis: Formulae for Continuous Size Distributions', *X-ray Spectrometry* **1**, 107–111.

Huovelin, J., Alha, L., Andersson, H., Andersson, T., Browning, R., Drummond, D., Foing, B., Grande, M., Hämäläinen, K., Laukkanen, J., Lämsä, V., Muinonen, K., Murray, M., Nenonen, S., Salminen, A.,

Sipilä, H., Taylor, I., Vilhu, O., Waltham, N. and Lopez-Jorkama, M. (2002), 'The SMART-1 X-ray solar monitor (XSM): calibrations for D-CIXS and independent coronal science', *Planetary and Space Science* **50**, 1345–1353.

Joy, K. H., Crawford, I. A., Kellett, B., Grande, M. N. and the C1XS Science Team (2008), The scientific case for the chandrayaan-1 x-ray spectrometer, *in* 'Lunar and Planetary Science XXXIX abstracts', p. 1070.

Lumme, K. and Bowell, E. (1981), 'Radiative transfer in the surfaces of atmosphereless bodies. I - Theory. II - Interpretation of phase curves', *Astronomical Journal* **86**, 1694–1721.

Maruyama, Y., Ogawa, K., Okada, T. and Kato, M. (2008), 'Laboratory measurements of particle size effect in x-ray fluorescence and implications to remote x-ray spectrometry of lunar regolith surface', *Earth, Planets and Space* **60**, 293–297.

McKay, D. S., Heiken, G., Basu, A., Blanford, G., Simon, S., Reedy, R., French, B. M. and Papike, J. J. (1991), *The lunar regolith*, Cambridge University Press, pp. 285–356.

Muinonen, K., Piironen, J., Shkuratov, Y. G., Ovcharenko, A. and Clark, B. E. (2002), 'Asteroid Photometric and Polarimetric Phase Effects', *Asteroids III* pp. 123–138.

Näränen, J., Kaasalainen, S., Peltoniemi, J., Heikkilä, S., Granvik, M. and Saarinen, V. (2004), 'Laboratory photometry of planetary regolith analogs. II. Surface roughness and extremes of packing density', *Astronomy & Astrophysics* **426**, 1103–1109.

Näränen, J., Parviainen, H. and Muinonen, K. (2007), X-ray fluorescence modelling for Solar system regoliths: Effects of viewing geometry, particle size, and surface roughness, *in* G. B. Valsecchi and D. Vokrouhlický, eds, 'IAU Symposium', Vol. 236 of *IAU Symposium*, pp. 243–250.

Nittler, L. R., McCoy, T. J., Clark, P. E., Murphy, M. E., Trombka, J. I. and Jarosewich, E. (2004), 'Bulk element compositions of meteorites: A guide for interpreting remote-sensing geochemical measurements of planets and asteroids', *Antarctic Meteorite Research* **17**, 233–253.

Nittler, L. R., Starr, R. D., Lim, L., McCoy, T. J., Burbine, T. H., Reedy, R. C., Trombka, J. I., Gorenstein, P., Squyres, S. W., Boynton, W. V., McClanahan, T. P., Bhangoo, J. S., Clark, P. E., Murphy, M. E. and

Killen, R. (2001), 'X-ray fluorescence measurements of the surface elemental composition of asteroid 433 Eros', *Meteoritics and Planetary Science* **36**, 1673–1695.

Okada, T. (2002), Surface elemental composition of asteroid 433 eros: Discussion on the results of the near/xgrs, *in* 'ISAS Lunar Planetary Symposium', Vol. 35 of *ISAS Lunar Planetary Symposium*, pp. 120–123.

Okada, T., Kato, M., Yamashita, Y., Shirai, K., Yamamoto, Y., Matsuda, T., Tsunemi, H. and Kitamoto, S. (2002), 'Lunar X-ray spectrometer experiment on the SELENE mission', *Advances in Space Research* **30**, 1909–1914.

Okada, T. and Kuwada, Y. (1997), Effect of surface roughness on X-ray fluorescence emission from planetary surfaces, *in* 'Lunar and Planetary Institute Conference Abstracts', Vol. 28 of *Lunar and Planetary Institute Conference Abstracts*, p. 1039.

Okada, T., Kuwada, Y. and Mizutani, H. (1998), Particle Size Effects in X-Ray Fluorescence: Implications for Planetary Missions, *in* 'Lunar and Planetary Institute Conference Abstracts', Vol. 29 of *Lunar and Planetary Institute Conference Abstracts*, p. 1597.

Okada, T., Shirai, K., Yamamoto, Y., Arai, T., Ogawa, K., Hosono, K. and Kato, M. (2006), 'X-ray Fluorescence Spectrometry of Asteroid Itokawa by Hayabusa', *Science* **312**, 1338–1341.

Parviainen, H. and Muinonen, K. (2007), 'Rough-surface shadowing of self-affine random rough surfaces', *Journal of Quantitative Spectroscopy and Radiative Transfer* **106**, 398–416.

Peck, L. C. and Smith, V. C. (1970), 'Quantitative chemical analysis of lunar samples', *Science* **167**, 532.

Rosato, A., Strandburg, K. J., Prinz, F. and Swendsen, R. H. (1987), 'Why the Brazil nuts are on top: Size segregation of particulate matter by shaking', *Physical Review Letters* **58**, 1038–1040.

Schlemm, C. E., Starr, R. D., Ho, G. C., Bechtold, K. E., Hamilton, S. A., Boldt, J. D., Boynton, W. V., Bradley, W., Fraeman, M. E., Gold, R. E., Goldsten, J. O., Hayes, J. R., Jaskulek, S. E., Rossano, E., Rumpf, R. A., Schaefer, E. D., Strohbehn, K., Shelton, R. G., Thompson, R. E., Trombka, J. I. and Williams, B. D. (2007), 'The X-Ray Spectrometer on the MESSENGER Spacecraft', *Space Science Reviews* **131**, 393–415.

Schulz, R. and Benkhoff, J. (2006), 'BepiColombo: Payload and mission updates', *Advances in Space Research* **38**, 572–577.

Sidky Mikhail, J. (1968), 'Color opposition effect of the lunar surface', *Icarus* **8**, 117–128.

Trucano, P. and Batterman, B. W. (1970), 'Effects of Porosity in Powder Diffraction', *Journal of Applied Physics* **41**(10), 3949–3953.

Warell, J. and Blewett, D. T. (2004), 'Properties of the Hermean regolith: V. New optical reflectance spectra, comparison with lunar anorthosites, and mineralogical modelling', *Icarus* **168**, 257–276.

Fraction of weight (%)		
Constituent	Olivine basalt	Apollo 11
SiO_2	44.9	40.0
MgO	21.8	7.9
Fe_2O_3	11.6	
FeO		19.1
Al_2O_3	10.1	10.2
CaO	5.7	11.3
Na_2O	2.9	0.4
TiO_2	2.0	10.5
K_2O	1.6	0.1
P_2O_5	0.5	0.1
MnO	0.2	0.3

Table 1: The chemical compositions of the finer-particle olivine basalt sample used in the present study (by courtesy of Derek Pullan, Space Research Center, University of Leicester and the Planetary Analogue Field Studies Network) and an olivine basalt sample from Apollo 11 landing site at Mare Tranquillitatis (Peck and Smith 1970).

rl	gs	og	rc	A	$B(10^{-4}/^{\circ})$	χ^2
Fe Kα/Ca Kα	$< 50\mu$m	$\epsilon = 0^{\circ}$	4.2%	0.99±0.02	8.7±5.1	0.19
Fe Kα/Ca Kα	$75 - 250\mu$m	$\epsilon = 0^{\circ}$	8.5%	0.99±0.02	20.0±5.4	0.22
Fe Kα/Ca Kα	$< 50\mu$m	$\iota = 0^{\circ}$	-7.7%	1.00±0.01	-14.4±4.2	0.16
Fe Kα/Ca Kα	$75 - 250\mu$m	$\iota = 0^{\circ}$	-2.0%	1.01±0.01	-4.5±4.1	0.48

Table 2: The relative intensity ratio changes of Fe Kα and Ca Kα lines for both viewing geometries and samples as presented in Figs. 10 and 11. The abbreviations in the table header are: ratioed lines (rl), particle-size range (gs), observation geometry (og), relative change (rc) over the angle-range of 0-50° obtained from the linear fit, parameters A and B of the linear least-squares fit of the form $y = A + B\alpha$ with their 1σ errors, and the reduced χ^2 values of the fits.

el	gs	og	R_0	k	η	χ^2
Fe Kα	$< 50\mu$m	$\epsilon = 0°$	2.73±0.44	0.012±0.035	1.80±0.43	1.11
Ca Kα	$< 50\mu$m	$\epsilon = 0°$	1.87±0.40	0.063±0.065	0.90±0.22	3.16
Fe Kα	$< 50\mu$m	$\iota = 0°$	2.21±0.36	-0.103±0.042	1.13±0.36	0.92
Ca Kα	$< 50\mu$m	$\iota = 0°$	2.53±0.60	0.015±0.039	1.50±0.63	1.99
Fe Kα	$75 - 250\mu$m	$\epsilon = 0°$	1.69±0.23	0.086±0.049	0.74±0.22	0.40
Ca Kα	$75 - 250\mu$m	$\epsilon = 0°$	1.66±0.26	-0.017±0.051	0.68±0.24	0.69
Fe Kα	$75 - 250\mu$m	$\iota = 0°$	2.47±0.95	-0.139±0.082	1.36±0.95	0.67
Ca Kα	$75 - 250\mu$m	$\iota = 0°$	3.64±1.82	-0.049±0.073	2.51±1.81	0.88

Table 3: The parameters R_0, k, and η obtained by fitting Fe Kα and Ca Kα intensities with the semiempirical function (Eq. 4). The parameter errors are 1σ errors for the optimum fit. The abbreviations are: emission line (el), particle-size range (gs), and observation geometry (og). The reduced χ^2 value of the optimum fit is also given.

Figure 1. The viewing geometry: ι, ϵ, and α are the incidence, emergence, and phase angles, and ϕ_0 and ϕ are the azimuth angles of the incident and emergent radiation, respectively.

Figure 2. The experimental setup. The view is from the top, i.e., the setup is horizontal. Measures in the setup are: the closest X-ray beam collimator-sample distance is 270 mm and the sample-detector distance is 140 mm. The detector head is offset from the center of the rotating arm by 10 mm to the direction of the X-ray source. The diameter and height of the cylindrical chamber are 650 mm and 300 mm, respectively. In this figure the setup is shown at $\iota = 0^\circ$ configuration.

Figure 3. Semi-empirical model spectrum of the X-ray source. The most noticeable features in the bremsstrahlung spectrum are the Titanium Kα and Kβ fluorescent emission lines at 4.51 keV and 4.93 keV, respectively, and the Titanium K absorption edge at 4.97 keV. The X-ray source is too luminous to be observed directly with the detector. The unit of intensity is arbitrary.

Figure 4. The measured spectrum of the <50 μm olivine basalt sample obtained at $\iota = 0^\circ$, $\epsilon = 21^\circ$ and the best fit with the multiple-Gaussian fitting model. All nine of the identified fluorescent emission lines have been marked.

Figure 5. The model spectrum deconvolved using the detector characteristics to show the actual X-ray fluxes from the sample.

Figure 6. The measured relative intensity ratios of several elemental fluorescent emission lines from a pellet made of olivine basalt with maximum particle size of 50 μm. The emergence angle is zero, i.e., the detector viewing direction is fixed perpendicular to the sample surface and the light source is moved. The error bars represent 1σ measurement errors. For plotting purposes, the elemental line ratios have been normalized to unity at $\iota = 9^\circ$ and vertically offset to separate the lines. The slopes are, however, comparable in the plot.

Figure 7. As in Fig. 6 for particle sizes 75-250 μm.

Figure 8. As in Fig. 6 but with the light source perpendicular to the sample surface and the detector moved.

Figure 9. As in Fig. 8 for particle sizes 75-250 μm.

Figure 10. The effect of particle size. Here the relative intensity ratios of Fe Kα and Ca Kα lines measured from both samples as a function of the incidence angle ($\epsilon = 0^\circ$) are presented. The results from the linear fitting are given in Table 2.

Figure 11. The same as Fig. 10 but with $\iota = 0^\circ$.

Figure 12. Absolute line intensities of Fe Kα emission fitted with the semiempirical function (Eq. 4). The results with $\iota = 0^\circ$ have been divided by $\cos\epsilon$ to normalize the measurement geometries.

Figure 13. The same as Fig. 12 but for Ca Kα emission.

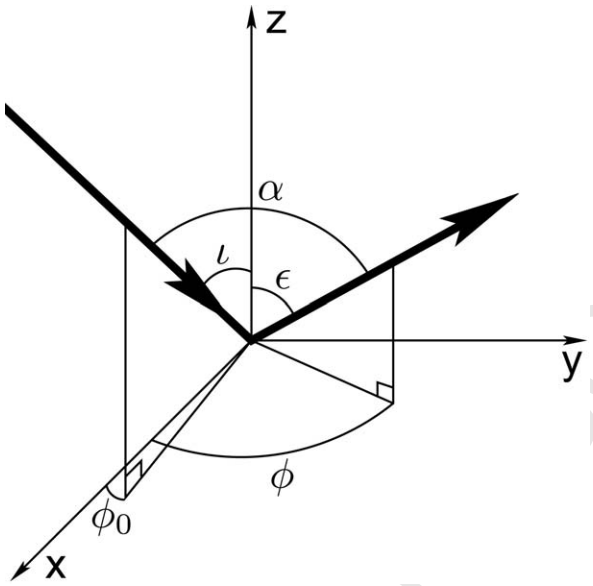

Figure 1:

.

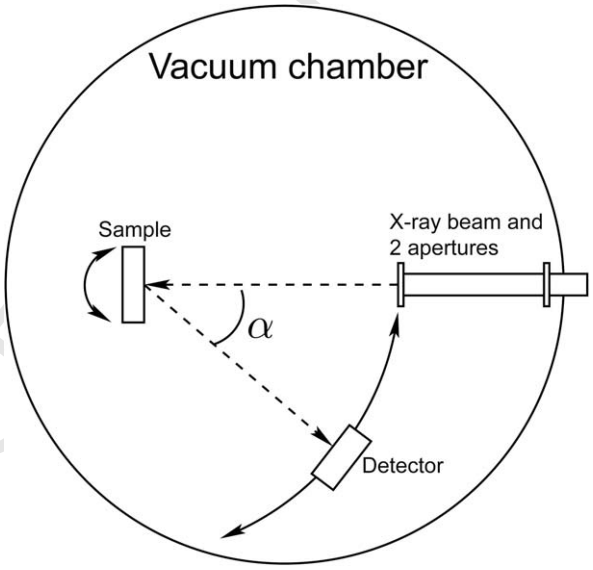

Figure 2:

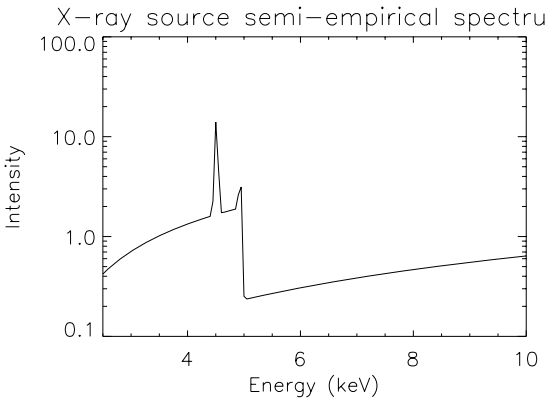

Figure 3:

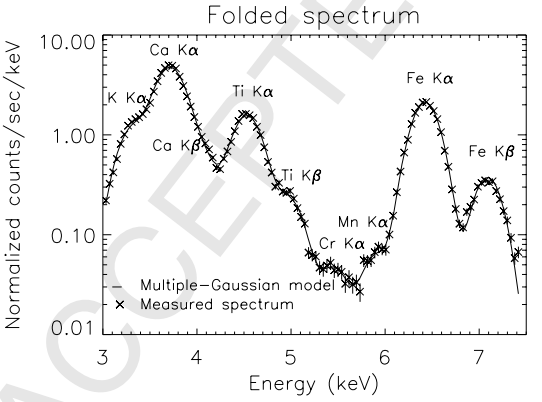

Figure 4:

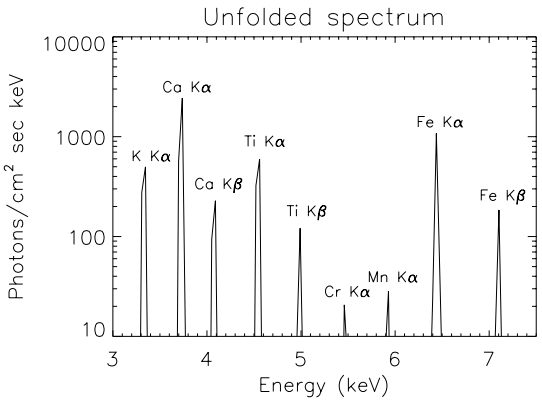

Figure 5:

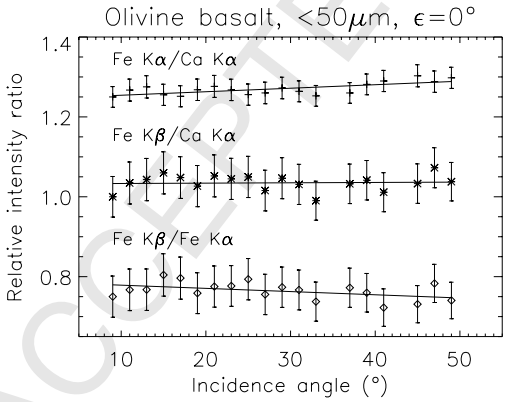

Figure 6:

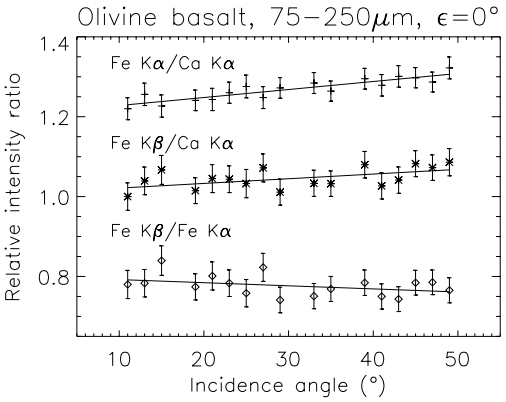

Figure 7:

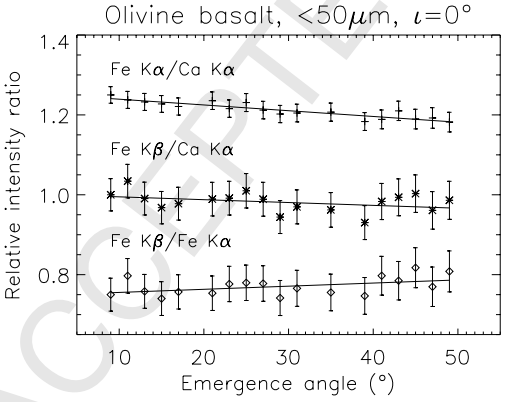

Figure 8:

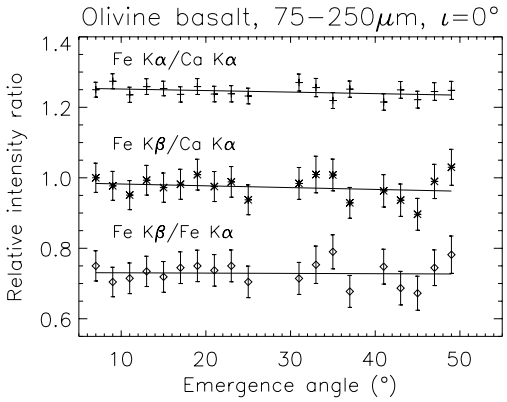

Figure 9:

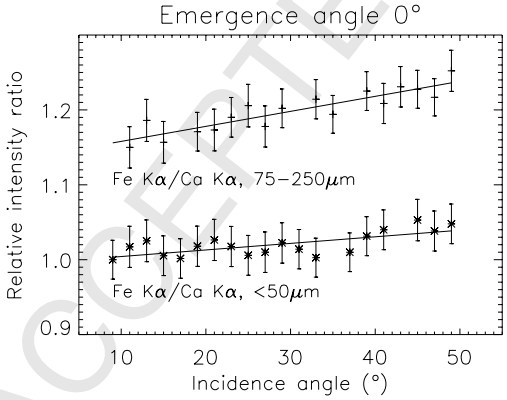

Figure 10:

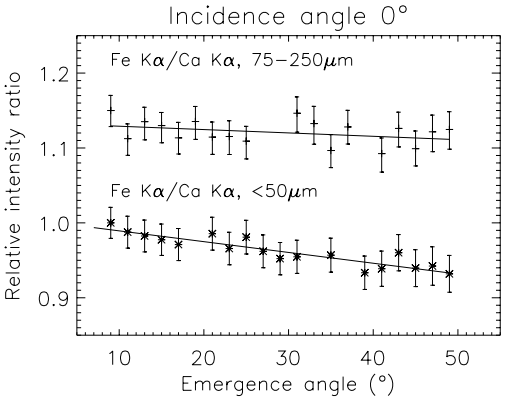

Figure 11:

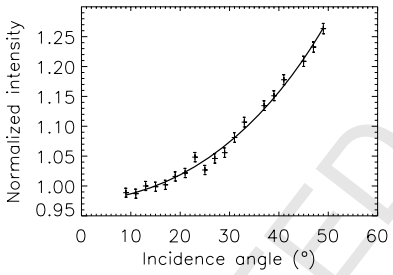

(a) $< 50\mu$m, $\epsilon = 0°$

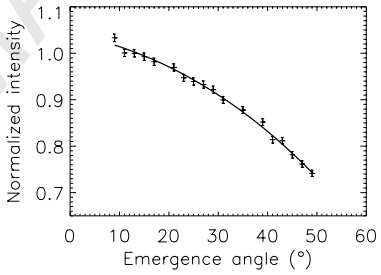

(b) $< 50\mu$m, $\iota = 0°$

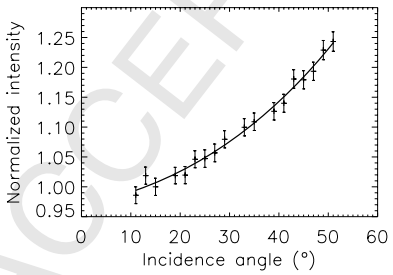

(c) $75 - 250\mu$m, $\epsilon = 0°$

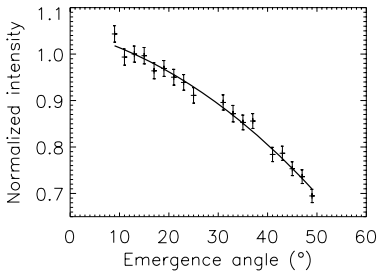

(d) $75 - 250\mu$m, $\iota = 0°$

Figure 12:

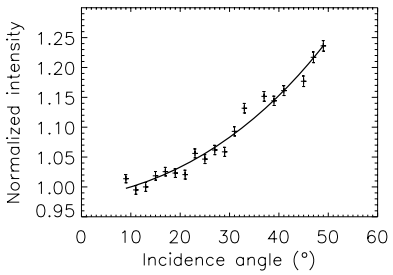

(a) $< 50\mu$m, $\epsilon = 0°$

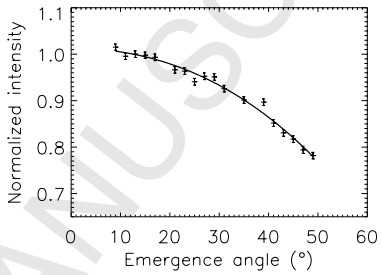

(b) $< 50\mu$m, $\iota = 0°$

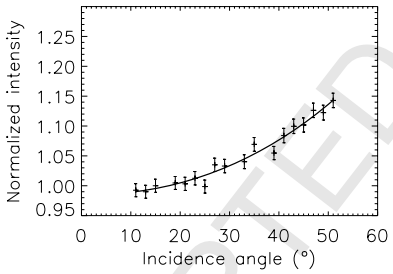

(c) $75 - 250\mu$m, $\epsilon = 0°$

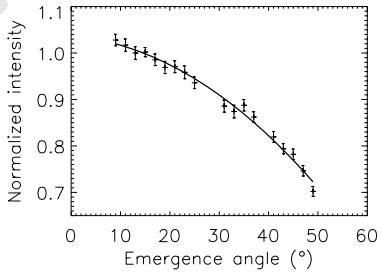

(d) $75 - 250\mu$m, $\iota = 0°$

Figure 13: